Advanced Optical Materials

ADVANCED OPTICAL MATERIALS
www.advopticalmat.de

RESEARCH ARTICLE OPEN ACCESS

White Light Emission and Energy Transfer in Mixed-Metal Europium/Terbium/Thulium Formate Metal–Organic Frameworks: Effect of Lanthanum Dilution

Leonardo E. Cruz-Estrada[1] | Irvin D. Villar-Gutiérrez[2] | Giuliano Giambastiani[3] | Ciro Falcony[2] | Silvia E. Castillo-Blum[1] | Andrea Rossin[4]

[1]Facultad de Química, Universidad Nacional Autónoma de México, CDMX, México | [2]Centro de Investigación y Estudios Avanzados del Instituto Politécnico Nacional, CDMX, México | [3]Dipartimento di Chimica "Ugo Schiff", Università di Firenze, Sesto Fiorentino, Italy | [4]Consiglio Nazionale delle Ricerche, Istituto di Chimica dei Composti Organometallici (ICCOM-CNR), Sesto Fiorentino, Italy

Correspondence: Silvia E. Castillo-Blum (blum@unam.mx) | Andrea Rossin (andrea.rossin@cnr.it)

Received: 18 March 2026 | **Revised:** 1 June 2026 | **Accepted:** 25 June 2026

Keywords: energy transfer | formates | lanthanides | luminescence | metal–organic frameworks (MOFs)

ABSTRACT

A series of mono-, bi-, tri- and tetrametallic lanthanide formate frameworks incorporating Eu^{3+}, Tb^{3+}, Tm^{3+} and La^{3+} were synthesized under solvothermal conditions and comprehensively characterized in the solid state. The compounds $[(Fmd)Ln(HCOO)_4]_n$ (Ln = Tb, Eu, Tm) are isostructural and crystallize in the orthorhombic space group $C222_1$, forming 3D formate-bridged frameworks with Ln–Ln separations of 6.6–6.8 Å, favorable for interionic energy transfer. Controlled incorporation of Eu^{3+} and Tb^{3+} enabled continuous color tuning from green to red through an efficient $Tb^{3+}\rightarrow Eu^{3+}$ energy-transfer process, reaching a maximum efficiency of 58.8% and quantum yields up to 70%. Introduction of Tm^{3+} provided blue emission, enabling RGB balance and near-white light generation in $[(Fmd)Eu_{0.475}Tb_{0.475}Tm_{0.05}(HCOO)_4]_n$, which exhibits CIE coordinates of (0.3198, 0.3027), a CCT of 6276 K and a CRI of 91. However, cross-relaxation processes reduced the quantum yield to 4%. To suppress concentration quenching, La^{3+} was introduced as a non-emissive diluent, yielding a trigonal $La(HCOO)_3$-based phase with improved quantum yield (26%) while preserving warm-white emission (CIE: 0.3389, 0.3591; CCT: 5256 K; CRI: 83). These results demonstrate the potential of lanthanide formate frameworks for studying energy-transfer phenomena and tailoring white-light emission through compositional engineering and rare-earth dilution strategies.

1 | Introduction

White light-emitting phosphors (WLEPs) have attracted considerable attention over the past decades due to their crucial role in modern optoelectronic technologies [1]. These materials are capable of emitting broadband white light either through a single-phase system or by combining emissions from multiple chromophores covering the entire visible spectrum [2]. Their efficient conversion of ultraviolet or blue excitation into white light makes them essential for solid-state lighting devices, such as white light-emitting diodes (WLEDs), as well as for displays, photonics, and bioimaging [3]. The development of efficient and stable WLEPs is driven by the global demand for energy-saving, environmentally friendly lighting sources that can replace traditional incandescent and fluorescent lamps [4]. Beyond lighting, white-emitting phosphors are relevant in optical sensing, [5] information encryption [6] and photocatalysis, [7] where precise color and intensity control is required. Consequently, the rational design of white light phosphors, along with the understanding of their structure–property relationship, continues to be a central

focus in materials chemistry and photophysics [8]. Among the strategies to achieve white emission, rare-earth-doped materials are particularly prominent [9]. Lanthanide ions (Ln^{3+}) offer tunable emission, high color purity, and excellent thermal and chemical stability. Their partially filled 4f orbitals ([Xe]$4f^n$, n = 0–14) give rise to multiple electronic levels responsible for sharp UV–vis–IR emissions originating from 4f–4f transitions, except for La^{3+} ($4f^0$) and Lu^{3+} ($4f^{14}$) [10]. The emissions from Eu^{3+}, Tb^{3+}, Tm^{3+}, Sm^{3+}, and Dy^{3+} ions correspond to red, green, blue, orange, and yellow emissions, respectively [11]. These bands exhibit high color purity because 4f–4f transitions are largely shielded from the chemical environment, resulting in narrow, positionally stable, metal-centred emissions [12–14]. Since 4f–4f transitions are forbidden, lanthanides exhibit low molar absorption coefficients, resulting in relatively low emission intensities [15]. However, certain ligands can transfer energy to lanthanide ions, thereby enhancing their emission intensity, a phenomenon known as the antenna effect [16, 17]. These characteristics have led to the synthesis of luminescent coordination compounds [18, 19] and metal-organic frameworks (MOFs); [20-24] in the latter case, lanthanide ions serve as nodes (Ln-MOFs) [25–28]. MOFs are crystalline porous materials formed by metal nodes and organic linkers, offering high structural tunability and design flexibility [29]. Their impact on materials chemistry was recognized with the 2025 Nobel Prize in Chemistry awarded to Susumu Kitagawa, Richard Robson, and Omar Yaghi for pioneering contributions to this field. MOFs provide a unique platform for WLEPs because multiple emissive centers can coexist within a well-defined framework, enabling broadband or multicomponent white emission [30]. This structural and photophysical tunability allows for precise control over chromaticity coordinates and color rendering index (CRI), which are key parameters for lighting and display applications [31]. Their hybrid nature combines the chemical robustness and high thermal stability of inorganic materials with the design versatility of organic systems. Moreover, MOFs can be processed into thin films, nanocrystals, or composites, facilitating their use in WLEDs, photonic coatings, and luminescent sensors [32–34]. Recent studies have indicated that in Ln-MOFs the modulation of the intermetallic distance between nodes, [35] the strategic mixing of different lanthanide ions at these nodes and the co-doping with metal-emissive ligands [36] represent effective approaches for synthesizing materials capable of functioning as white phosphors. Such materials show significant promise for application in WLEDs [37]. A key advantage of Ln-MOFs over luminescent transition metal MOFs is their ability to generate a wide range of emission colors with high color purity [38]. In contrast, transition metal MOFs typically exhibit broad emissions arising from ligands or ligand to metal charge transfers, which usually fall within the blue or UV spectrum [39]. Full- or empty-shell cations such as Zn^{2+}, Cd^{2+}, Ag^{+}, or Zr^{4+} are commonly employed to avoid d–d transitions [40, 41]. Trimetallic Ln-MOFs incorporating Eu^{3+}, Tb^{3+}, and Gd^{3+} capable of white emission are relatively scarce [42–45]. More commonly, Eu^{3+}, Tb^{3+}, and Tm^{3+} are used as dopants in glasses [46–48] and inorganic matrices [49–55] to achieve white light by adjusting their relative proportions. This approach exploits the red emission of Eu^{3+} ($^5D_0 \rightarrow {}^7F_2$), the green emission of Tb^{3+} ($^5D_4 \rightarrow {}^7F_5$), and the blue emission of Tm^{3+} ($^1G_4 \rightarrow {}^3H_6$ or $^1D_2 \rightarrow {}^3F_4$) [56, 57]. While varying Eu^{3+}/Tb^{3+} ratios readily tunes emission from green to red, the introduction of Tm^{3+} increases the risk of concentration quenching through cross-relaxation, particularly at high dopant levels [58]. To mitigate this issue, non-emissive ions like La^{3+} are often exploited to "dilute" the emissive ions, effectively reducing their proximity and preventing cross-relaxation [59, 60]. Previous studies reported lanthanide-based polymeric formates formed via in situ hydrolysis of DMF or formamide under moderately acidic conditions, generating formate linkers [61, 62]. Subsequent investigations indicate that the hydrolysis of formamide under solvothermal conditions is significantly influenced by temperature. Within the 50°C–70°C range, formamide serves as a ligand that coordinates to lanthanide ions. Conversely, at temperatures exceeding 100°C it is transformed into formamidine, resulting in the in situ generation of the formamidinium cation [63, 64]. The formate anions, despite being relatively small ligands, effectively link the lanthanides while maintaining an optimal distance that prevents cross-relaxation. In 2012, some of us synthesized polymeric formates with the general formula $[(Fmd)Ln(HCOO)_4]_n$ [Fmd^+ = formamidinium ion, $HC(NH_2)_2^+$], observing that those containing Tb^{3+} and Eu^{3+} exhibited significant luminescence, even though formate is not an effective chromophore [65]. The quantum yield (φ) of the Tb^{3+}compound was 83% when excited at 368 nm ($^7F_6 \rightarrow {}^5L_{10}$). In this study, we synthesized new lanthanide formate frameworks with Tb^{3+} (**1**), Eu^{3+} (**7**), and Tm^{3+} (**8**) that are isostructural with those previously reported for Dy^{3+} [65]. Bimetallic compounds $[(Fmd)Eu_xTb_{1-x}(HCOO)_4]_n$ (**2–6**) enabled controlled color modulation from green to red. A trimetallic $Eu^{3+}/Tb^{3+}/Tm^{3+}$ compound (**9**) was also prepared, and white emission was achieved in a tetrametallic derivative (**10**) by diluting the emissive ions with La^{3+}. All compounds were characterized by single-crystal and powder x-ray diffraction, infrared spectroscopy, thermogravimetric and elemental analyses, and scanning electron microscopy. Their solid-state luminescent properties were investigated by emission spectroscopy. Importantly, this study reports for the first time to our knowledge an energy transfer analysis involving formate, Tb^{3+}, Eu^{3+}, and Tm^{3+} within a MOF matrix.

2 | Material and Methods

2.1 | Materials

All reagents and solvents were used without further purification. Cyclobutane-1,1'-dicarboxylic acid ($C_6H_8O_4$, 99%), formamide (CH_3NO, ≥99.0%), europium(III) nitrate pentahydrate ($Eu(NO_3)_3{\cdot}5H_2O$, 99.9%), terbium(III) nitrate pentahydrate ($Tb(NO_3)_3{\cdot}5H_2O$, 99.9%), thulium(III) nitrate pentahydrate ($Tm(NO_3)_3{\cdot}5H_2O$, 99.9%), and lanthanum(III) nitrate hexahydrate ($La(NO_3)_3{\cdot}6H_2O$, 99.9%) were purchased from Sigma–Aldrich. Ethanol (EtOH) and diethyl ether ($(C_2H_5)_2O$) were purchased from J.T. Baker.

2.2 | Physical Measurements

Fourier transform infrared (FT-IR) spectra were recorded on a Perkin Elmer Spectrum 400 spectrometer equipped with a reflectance ATR accessory. Scanning electron microscopy (SEM) measurements were performed with a JEOL JSM-5910 and an energy dispersive spectroscopy (EDS) microanalysis on an Oxford Aztec 100 spectrometer. Powder x-ray diffraction (PXRD) was recorded on a Bruker D8 Advance diffractometer. Excitation and

emission spectra were measured on a Perkin Elmer Fluorescence Spectrometer FL8500. The luminescent decay curves were recorded at room temperature on a SpectraPro 2300i monochromator using a Hamamatsu accessory, a chopper controller Stanford Research SR540 (At 150 Hz), and an oscilloscope, Teledyne Lecroy HD4096, which was used (lifetimes were obtained by fitting integrated photoluminescence decay curves with a mono-exponential function ($y = y_0 + A_1 e^{-x/t1}$)). The QY and emission spectra were determined using the FLS980-Spectrometer with 200–400 nm UV filters using the integrating sphere method. ICP-OES analysis was performed using open digestions of the samples, dissolving them in concentrated HNO_3. Subsequently, they were analyzed using a calibration curve with a 1000 µg/mL HPS lanthanide ion multi-element standard on a Thermo Scientific iCAP 7000 Series instrument, with a Teledyne CETACT U5000AT+ ultrasonic nebulizer and an ASX-280 autosampler. The CIE 1931 diagrams were calculated using ColorCalculator software v 7.77. PXRD qualitative measurements were carried out in the 2°–50° 2θ region with a Panalytical X'PERT PRO diffractometer equipped with a Ni filter on the diffracted beam, a PIXcel solid state detector and a sealed x-ray tube (Cu Kα, λ = 1.5418 Å). Slits were used on both the incident (Soller slits aperture: 0.25°; divergence slit aperture: 0.5°) and the diffracted (anti-scatter slit aperture: 7.5 mm) beam. The generator was operated at 40 kV and 40 mA. Solid-state UV–vis absorption diffuse reflectance spectra were recorded from 250 to 600 nm using a Jasco V-770 spectrophotometer equipped with a 60 mm integrating sphere and a PbS detector (ISN-923), at 1 nm intervals. Solid-state fluorescence spectra were obtained on a JascoFP-8300 spectrofluorometer equipped with a 150 W Xenon arc lamp. The samples were irradiated at the maximum absorption wavelength. Thermogravimetric analyses (TG-DTG) were performed under a N_2 flow (100 mL min^{-1}) at a heating rate of 5 K min^{-1} with an EXSTAR Thermo Gravimetric Analyzer Seiko 6200. The latter was coupled with a ThermoStarTM GSD 301T mass spectrometer for mass analysis of the volatile species.

2.3 | Synthesis

The synthesis procedure with Tb^{3+} (**1**) is described as a representative example: Cyclobutane-1,1'-dicarboxylic acid (0.2059 g, 1.4 mmol) and terbium(III) nitrate pentahydrate (1.2180 g, 2.8 mmol) were dissolved in 5 mL of formamide. The solution was then transferred to a 15 mL Teflon beaker placed in an autoclave and heated in the oven at 130°C for 24 h. Afterward, the reaction was allowed to cool slowly overnight until it reached room temperature. Upon opening the autoclave, the formation of colorless crystals of **1** was observed. These crystals were vacuum-filtered and washed with ethanol (4 × 10 mL) and diethyl ether (4 × 10 mL). Finally, the crystals were dried under a nitrogen flow for 2 h. For compounds containing mixtures of lanthanide ions, the proportions indicated in Table 1 were added to the reaction mixture to ensure that the total amount of lanthanides in each compound equals 2.8 mmol.

Ln = Tb (1) Yield: 0.7174 g (66%, based on terbium). Anal. Calcd. for **1**, $C_5H_9N_2O_8Tb$ (384.06 g/mol): C, 15.64; H, 2.36; N, 7.29. Found: C, 16.18; H, 2.31; N, 7.48. IR bands (ATR, cm^{-1}) for **1**: 3334 m [ν(N—H) formamidinium]; 2849 m [ν(C—H) formate]; 1722 m and 1587 vs [$\nu(COO^-)$]; 1362 s [ν(C—N)]; 1119 w, 786 m [γ(C—H)], 719 m, 533 w. Figure S1.

TABLE 1 | Labels of the main synthesized compounds.

Lanthanide formate framework	Compound
$[(Fmd)Tb(HCOO)_4]_n$*	1
$[(Fmd)Eu_{0.01}Tb_{0.99}(HCOO)_4]_n$	2
$[(Fmd)Eu_{0.05}Tb_{0.95}(HCOO)_4]_n$	3
$[(Fmd)Eu_{0.10}Tb_{0.90}(HCOO)_4]_n$	4
$[(Fmd)Eu_{0.30}Tb_{0.70}(HCOO)_4]_n$	5
$[(Fmd)Eu_{0.50}Tb_{0.50}(HCOO)_4]_n$*	6
$[(Fmd)Eu(HCOO)_4]_n$*	7
$[(Fmd)Tm(HCOO)_4]_n$	8
$[(Fmd)Eu_{0.475}Tb_{0.475}Tm_{0.05}(HCOO)_4]_n$*	9
$[Eu_{0.0475}Tb_{0.0475}Tm_{0.005}La_{0.9}(HCOO)_3]_n$*	10
$La(HCOO)_3$	11

*Table S1 for the quantification of lanthanide elements in selected samples, as determined by ICP-OES.

Ln = Eu and Tb (6). Yield: 0.5555 g (52%, based on the metals) Anal. Calcd. for **6**, $C_5H_9N_2O_8Eu_{0.50}Tb_{0.50}$ (380.58 g/mol): C, 15.78; H, 2.38; N, 7.34. Found: C, 16.12; H, 2.41; N, 7.53. IR bands (ATR, cm^{-1}) for **6**: 3329 m [ν(N—H) formamidinium]; 2844 m [ν(C—H) formate]; 1722 m and 1587 vs [$\nu(COO^-)$]; 1355 s [ν(C—N)]; 1119 w, 792 m [γ(C—H)], 724 m, 527 w. Figure S1.

Ln = Eu (7) Yield: 0.7242 g (67%, based on europium). Anal. Calcd. for **7**, $C_5H_9N_2O_8Eu$ (377.10 g/mol): C, 15.92; H, 2.41; N, 7.43. Found: C, 16.20; H, 2.40; N, 7.52. IR bands (ATR, cm^{-1}) for **7**: 3329 m [ν(N—H) formamidinium]; 2838 m [ν(C—H) formate]; 1722 m and 1587 vs [$\nu(COO^-)$]; 1362 s [ν(C—N)]; 1119 w, 787 m [γ(C—H)], 719 m, 533 w. Figure S1.

Ln = Tm (8) Yield: 0.7268 g (67%, based on thulium). Anal. Calcd. for **8**, $C_5H_9N_2O_8Tm$ (394.07 g/mol): C, 15.24; H, 2.30; N, 7.11. Found: C, 15.79; H, 2.28; N, 7.29. IR bands (ATR, cm^{-1}) for **8**: 3323 m [ν(N—H) formamidinium]; 2855 m [ν(C—H) formate]; 1728 m and 1592 vs [$\nu(COO^-)$]; 1367 s [ν(C—N)]; 1119 w, 798 m [γ(C—H)], 725 m, 527 w. Figure S1.

Ln = Eu, Tb and Tm (9). Yield: 0.7402 g (68%, based on the metals). Anal. Calcd. for **9**, $C_5H_9N_2O_8Eu_{0.475}Tb_{0.475}Tm_{0.05}$ (381.25 g/mol): C, 15.75; H, 2.38; N, 7.35. Found: C, 15.93; H, 2.50; N, 7.39. IR bands (ATR, cm^{-1}) for **9**: 3329 m [ν(N—H) formamidinium]; 2844 m [ν(C—H) formate]; 1722 m and 1587 vs [$\nu(COO^-)$]; 1362 s [ν(C—N)]; 1119 w, 792 m [γ(C—H)], 719 m, 533 w. Figure S1.

Ln = Eu, Tb, Tm and La (10). Yield: 0.7272 g (95%, based on the metals). Anal. Calcd. for **10**, $C_3H_3O_6Eu_{0.0475}Tb_{0.0475}Tm_{0.005}La_{0.9}$ (275.68 g/mol): C, 13.07; H, 1.09. Found: C, 14.25; H, 1.51. IR bands (ATR, cm^{-1}) for **10**: 1564 m and 1398 vs [$\nu(COO^-)$]; 1351 s [δ(C—H)]; 774 m [γ(C—H)], 719 m, 533 w. Figure S1.

TABLE 2 | Crystallographic data and structure refinement details for selected isostructural lanthanide formate frameworks.

Compound	$[(Fmd)Tb(HCOO)_4]_n$	$[(Fmd)Eu(HCOO)_4]_n$	$[(Fmd)Tm(HCOO)_4]_n$	$[(Fmd)Eu_{0.50}Tb_{0.50}(HCOO)_4]_n$
Label	1	7	8	6
Empirical formula	$C_5H_9O_8N_2Tb$	$C_5H_9O_8N_2Eu$	$C_5H_9O_8N_2Tm$	$C_5H_9O_8N_2Eu_{0.31}Tb_{0.69}$
Formula weight	384.06 g/mol	377.10 g/mol	394.07 g/mol	380.58 g/mol
Temperature	−173°C	−173°C	−173°C	−173°C
Wavelength	0.71073 Å	0.71073 Å	0.71073 Å	1.5418 Å
Crystal system	Orthorhombic	Orthorhombic	Orthorhombic	Orthorhombic
Space group	$C222_1$	$C222_1$	$C222_1$	$C222_1$
Unit cell dimensions	$a = 7(2)$ Å	$a = 6.714$ Å	$a = 6.622$ Å	$a = 6.698$ Å
	$b = 19(6)$ Å	$b = 18.696$ Å	$b = 18.334$ Å	$b = 18.605$ Å
	$c = 8(2)$ Å	$c = 8.531$ Å	$c = 8.392$ Å	$c = 8.497$ Å
Volume	1051 $Å^3$	1070.8 $Å^3$	1018.9 $Å^3$	1058.8 $Å^3$
Z	4	4	4	4
Density (calculated)	2.427 Mg/m^3	2.339 Mg/m^3	2.569 Mg/m^3	2.387 Mg/m^3
Absorption coefficient	6.760 mm^{-1}	5.888 mm^{-1}	8.740 mm^{-1}	37.998 mm^{-1}
F(000)	728	720	744	724
Goodness of fit on F2	1.068	1.035	1.049	1.138
Final R indices [I>2sigma(I)]	R1 = 0.0174 wR2 = 0.0405	R1 = 0.0182 wR2 = 0.0445	R1 = 0.0226 wR2 = 0.0556	R1 = 0.0366 wR2 = 0.0922
R indices (all data)	R1 = 0.0176 wR2 = 0.0406	R1 = 0.0191 wR2 = 0.0450	R1 = 0.0233 wR2 = 0.0561	R1 = 0.0378 wR2 = 0.0931

2.4 | Structure Determination from Single-Crystal X-ray Diffraction

Single crystal x-ray diffraction data for **1**, **6**, **7** and **8** were collected at low temperature (T = −173°C) on 0.01 × 0.02 × 0.03 mm^3 colorless prisms using a Bruker APEX-II CCD diffractometer equipped with a sealed x-ray source (Cu Kα, $\lambda = 1.5418$ Å; Mo Kα, $\lambda = 0.71073$ Å). Direct methods, as implemented in Sir2014, [66] were used to solve the crystal and molecular structure. Structure refinement was then performed by full-matrix least-squares against F^2, as implemented in SHELXL-2018 [67]. All the non-hydrogen atoms were refined anisotropically, while the hydrogen atoms were fixed in calculated positions (adopting the riding model) and refined isotropically with $U_{iso} = 1.2U_{eq}$(C) (C = carbon atom to which the H atom is bound). The geometrical calculations were performed by PARST97, [68] CCDC 2537337, 2537336, 2537338 and 2537339 contain the supplementary crystallographic data. These data can be obtained free of charge from The Cambridge Crystallographic Data Centre via https://www.ccdc.cam.ac.uk/structures/. Table 2 collects the main experimental details and crystallographic data.

3 | Results and Discussion

3.1 | Structure Description of the Lanthanide Formate Frameworks

Following the solvothermal synthesis described in Section 2.3, crystals suitable for x-ray diffraction analysis were obtained. The compounds $[(Fmd)Tb(HCOO)_4]_n$ (**1**), $[(Fmd)Eu(HCOO)_4]_n$ (**7**) and $[(Fmd)Tm(HCOO)_4]_n$ (**8**) are isostructural and crystallize in an orthorhombic crystal system with a *C222₁* chiral space group. As an example, the crystal structure of the compound **7** is presented in Figure 1. Each Eu^{3+} ion exhibits a coordination number of eight, characterized by a square antiprism geometry. The Eu^{3+} ion is coordinated by eight oxygen atoms, which originate from four formate molecules that serve as bridges, creating an anionic 3D lanthanide formate framework. A Eu^{3+} ion and a formamidinium molecule balance the −4 charge from the four formate molecules. The formamidinium cations are generated by formamide hydrolysis catalyzed by cyclobutane-1,1'-dicarboxylic acid (as previously observed for the Dy^{3+} analogue) [65] and they are located within the pores of the framework.

Table 2 presents the crystallographic and refinement data for compounds **1**, **6**, **7**, and **8**. A comparison of these data with the previously reported crystal of the dysprosium compound [65] reveals that compounds **1**, **7**, and **8** are isostructural, as they share the same empirical formula and space group *C222₁*. It is noteworthy that the cell volume decreases in accordance with the lanthanide ionic radius, following the trend $Eu^{3+} > Tb^{3+} > Tm^{3+}$, which aligns with the lanthanide contraction phenomenon [69]. The bimetallic compound **6** is also isostructural to the others; however, the refinement required the use of the Cu wavelength (CuKα = 1.5418 Å) due to the presence of twinned crystals. The unit cell volume of compound **6** is nearly an average of the cell volumes of compounds **1** and **7**, as this compound consists of a mixture of Eu^{3+} and Tb^{3+}. In the analysis of compound **6**, measured distances between nodes fall within the average range established by their respective monometallic structures ($d_{Ln\text{-}Ln}$ =

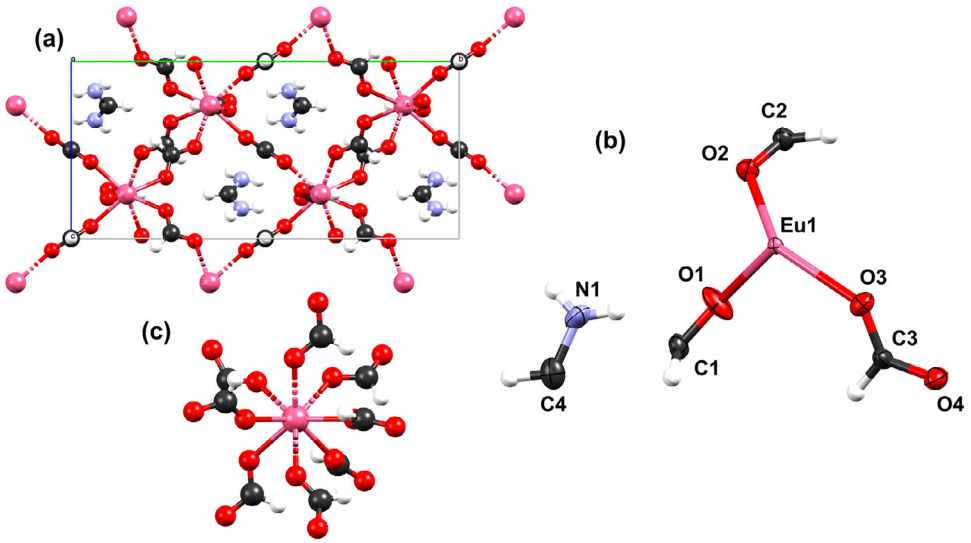

FIGURE 1 | Crystal structure of $[(Fmd)Eu(HCOO)_4]_n$: (a) Unit cell viewing from a axis, (b) asymmetric unit with anisotropic displacements ellipsoids drawn at the 90% of probability level, (c) coordination sphere of Eu^{3+}.

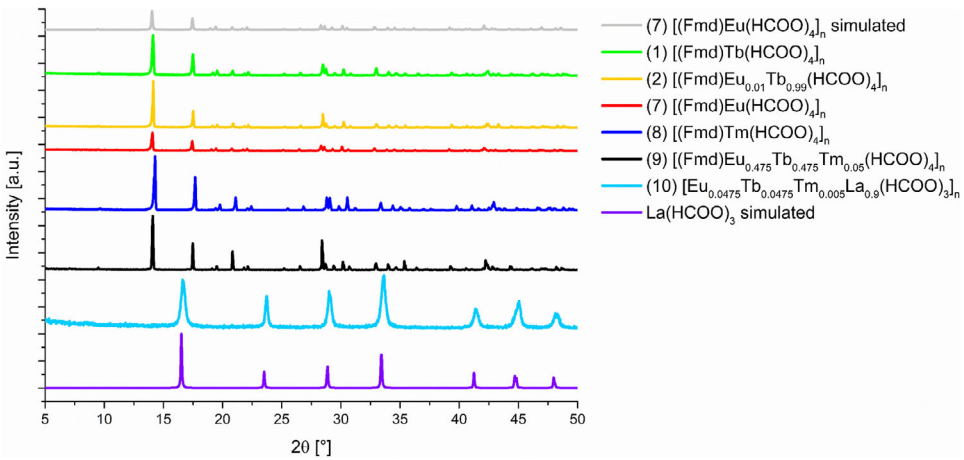

FIGURE 2 | Room temperature powder x-ray diffractograms (5°–50° 2θ range) of the main compounds presented in this work at comparison.

6.698, 6.722, and 6.803 Å). Interestingly, although a stoichiometric mixture of 50% Eu^{3+} and 50% Tb^{3+} was initially employed for the synthesis, the refinement of the metal site occupancy from X-ray diffraction analysis indicated that the actual metal proportion deviates from the initial reactants' composition, resulting in 31% Eu^{3+} and 69% Tb^{3+} in the crystal. The minimum distances between the lanthanide ions in each crystal are as follows: $d_{Eu\text{-}Eu}$ = 6.714 Å for **7**, $d_{Tb\text{-}Tb}$ = 6.694 Å for **1**, and $d_{Tm\text{-}Tm}$ = 6.622 Å for **8**.

The diffractograms presented in Figure 2 indicate that compounds **1**, **6**, **7**, **8** and **9** exhibit the same crystallographic phase. The simulated diffractogram for the single crystal of the Eu^{3+} compound (**7**) aligns closely with the experimental diffractograms. In the case of compound **2**, containing a 1:99 Eu:Tb ratio (Figure 2 – yellow line), it is important to note that it is not a physical blend of two homometallic phases but it is a genuine bimetallic derivative; the absence of doubled peaks in the diffractogram supports this conclusion [70]. Besides, all the bimetallic compounds with general formula $[(Fmd)Eu_xTb_{1-x}(HCOO)_4]_n$ share the same crystal structure (Figure S2). Additionally, the peaks observed in the Tm^{3+} compound (**8**) are more intense, attributed to the Tm^{3+} ion acting as a heavy atom that enhances X-ray diffraction due to its higher electron count, in contrast to the other lanthanides [71]. The diffractograms corresponding to the trimetallic compounds with the general formula $[(Fmd)Eu_xTb_yTm_{1-x-y}(HCOO)_4]_n$ are presented in Figure S3. These results indicate that all compounds exhibit uniform structural features and share the same crystalline phase.

Intriguingly, the introduction of La^{3+} in the synthesis causes a complete phase change, leading to the exclusive formation of trigonal $La(HCOO)_3$ (space group *R3m*). Indeed, the diffraction peaks found for the tetrametallic compound (**10**) correspond precisely with those of the simulated crystal structure of $La(HCOO)_3$ [72, 73]. La^{3+} with its larger ionic radius compared to the other lanthanides possibly prevents the incorporation of the formamidinium ion into the voids of the network. The observed

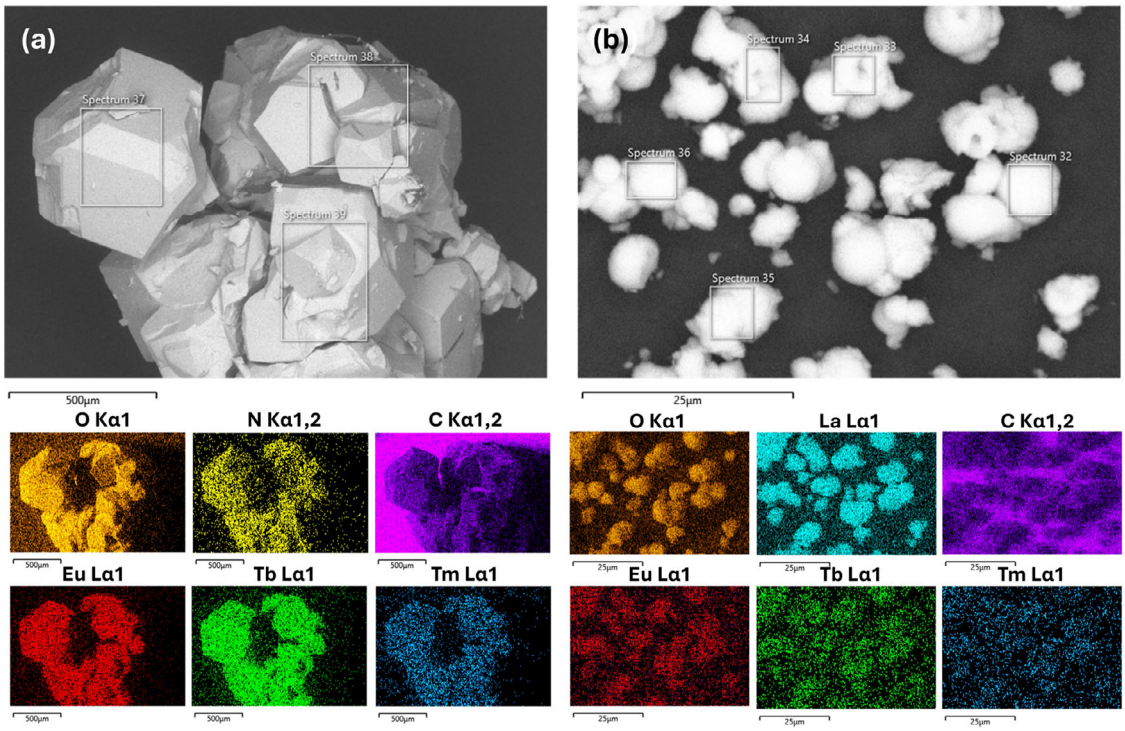

FIGURE 3 | SEM micrographs and EDS maps for compounds 9 (a) and 10 (b).

peak broadening in the diffractogram of **10** witnesses its lower crystallinity if compared with **1**–**9**.

3.2 | SEM-EDS Studies

Figure 3 shows the SEM micrographs and related EDS analysis of **9** and **10**. The images reveal that **9** is microcrystalline, with microcrystals exhibiting a regular prismatic morphology; however, intergrowth is observed among the crystals. EDS mapping demonstrates homogeneous element distribution on the microcrystal's surface. Notably, Eu^{3+} and Tb^{3+} represent approximately 15% of the surface composition, while the Tm^{3+} ion is found at about 1.8%, as indicated by the EDS spectra shown in Figure S4a. These percentages align well with the amounts that were initially employed in the synthesis. In contrast, **10** displays a markedly different morphology, lacking the regular structure of its ionic homologues, which suggests a loss of crystallinity, likely due to the presence of the La^{3+} ion [74] and formation of $La(HCOO)_3$. La^{3+} is found to cover 31% of the surface composition, while Eu^{3+} and Tb^{3+} are present at approximately 1.5% and Tm^{3+} is observed only at 0.2%, according to the EDS spectra in Figure S4b. This correlates with the observation that these ions are "diluted" ca. tenfold in **10** compared to **9**.

3.3 | Thermal Stability

As a representative example, the thermogram depicted in Figure 4a illustrates the thermal decomposition process of $[(Fmd)Eu_{0.5}Tb_{0.5}(HCOO)_4]_n$ (**6**). The formation of the intermediate $Ln(HCOO)_3$ is observed between T = 250°C and 320°C [weight loss = 23.3% (calculated); 24.3% (experimental)]. Real-time mass analysis indicates the production of formic acid and formamidine, with detectable signals at T = 223°C and 357°C (m/z = 45, 46, and 47). Ultimately, the corresponding lanthanide oxides are formed above T = 600°C [total weight loss = 52.7% (calculated); 52.8% (experimental)]. This analysis is consistent with those previously reported for Mg [75] and Gd [65] compounds. This thermal behavior is common to all compounds in the series, with slightly different decomposition temperatures related to the strength of the Ln-formate bond. The thermogram of compound **10**, as illustrated in Figure 4b, exhibits a distinct thermal behavior when compared to compounds **6** and **9**, additional proof of evidence of its different chemical composition. The thermal decomposition pathway of compound **10** is characterized by the generation of formic acid at the first thermal event at T = 350°C and subsequent formation of lanthanide oxides after decomposition (T ≥ 650°C).

3.4 | Luminescent Properties

3.4.1 | Mono and Bimetallic Lanthanide Formate Frameworks with Eu^{3+}, $Tb^{3+}$and Tm^{3+}

The absorption, excitation, and emission spectra of **1**, **2**, and **7** are illustrated in Figure 5. The metal centers primarily dictate their optical properties, since formate and formamidinium are not involved in emission processes between λ = 500 and 750 nm; [76] formate shows absorption and emission mainly in the UV region [77]. Notably, these lanthanide ions can be efficiently excited at the specific wavelengths λ_{ex} = 368 nm [78] for Tb^{3+} and λ_{ex} = 395 nm [79] for Eu^{3+} to trigger their corresponding emissions. It is important to recognise that the absorption bands of the lanthanides exhibit significant coincidence and overlap with their respective excitation bands. Consequently, all the

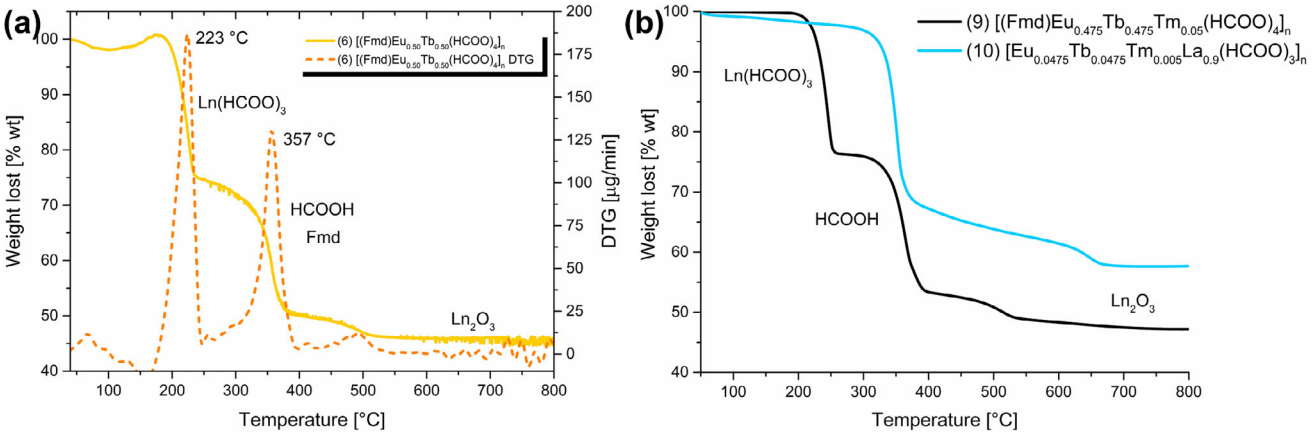

FIGURE 4 | TGA-DTG profile of 6(a), 9 and 10 (b).

radiation absorbed during the excitation process is subsequently utilized for emission. For compound **1**, the excitation spectrum (dark green line) is predominantly characterized by the excitation bands of Tb^{3+}, with a significant transition at $\lambda = 368$ nm ($^7F_6 \rightarrow {}^5L_{10}$). The emission spectrum (green line, Figure 5a) further corroborates the distinctive 4f-4f transitions associated with Tb^{3+}, showcasing the highest emission intensity observed among the compounds studied. In contrast, the excitation spectrum for compound **7** (dark red line) reveals excitation exclusively from the Eu^{3+} metal. The most pronounced excitation band corresponds to the $^7F_0 \rightarrow {}^5L_6$ transition of Eu^{3+}, observed at $\lambda = 395$ nm. The emission spectrum (red line, Figure 5c) exhibits only the 4f–4f transition bands of the Eu^{3+} ion. Notably, the Eu^{3+} ions within this compound are localised in a centrosymmetric environment, as confirmed by single crystal x-ray diffraction analysis (Figure 1c). This structural arrangement accounts for the observed intensity disparity between the transitions, where the $^5D_0 \rightarrow {}^7F_1$ transition is larger than $^5D_0 \rightarrow {}^7F_2$, and the absence of the $^5D_0 \rightarrow {}^7F_0$ transition is noteworthy [80, 81]. The predominant transition at $\lambda = 593$ nm yields an orange emission, which is distinctly different from the typical red-orange emission observed when the $^5D_0 \rightarrow {}^7F_2$ transition is dominant. In the case of the bimetallic compound **2**, analysis of the emission spectrum (yellow line, Figure 5b) reveals a light-yellow emission, with a composition ratio of 1:99 Eu^{3+}:Tb^{3+}. This spectrum encompasses the 4f-4f transitions from both lanthanides, with the $^5D_4 \rightarrow {}^7F_5$ transition of Tb^{3+} (green emission at $\lambda = 545$ nm) being the most intense. The subsequent emissions correspond to the $^5D_0 \rightarrow {}^7F_1$ bands (yellow emission at $\lambda = 593$ nm) and the $^5D_0 \rightarrow {}^7F_2$ bands (red-orange emission at $\lambda = 618$ nm) of Eu^{3+}. Additionally, the $^5D_4 \rightarrow {}^7F_6$ band (cyan emission at $\lambda = 490$ nm) of Tb^{3+} is also observed. Crucially, upon direct excitation of Tb^{3+} at $\lambda_{ex} = 368$ nm (via the $^7F_6 \rightarrow {}^5L_{10}$ transition), emission bands from both lanthanides are detected, indicating an energy transfer from Tb^{3+} to Eu^{3+}, where Tb^{3+} effectively acts as an antenna for Eu^{3+} [82, 83]. This energy transfer is remarkably efficient, sustaining the noted 1:99 ratio of Eu^{3+}:Tb^{3+}. These findings underscore the potential of tuning luminescent properties in lanthanide-based materials for advanced applications in photonics and optoelectronics.

In the quest to optimize the yellow emission of the compounds $[(Fmd)Eu_xTb_{1-x}(HCOO)_4]_n$, the color was adjusted by varying the ratio of Eu^{3+} and Tb^{3+} ions from compounds **1** to **7**. The emission spectra presented in Figure 6 reveal that as the Eu^{3+} content changes, the intensity of the Tb^{3+} hypersensitive transition band ($^5D_4 \rightarrow {}^7F_5$) decreases, while those of the $^5D_0 \rightarrow {}^7F_1$ and $^5D_0 \rightarrow {}^7F_2$ bands of Eu^{3+} increase. This observation indicates an energy transfer from Tb^{3+} to Eu^{3+}. Additionally, the CIE diagram illustrates a linear trend in color modulation when both lanthanides are combined. The excitation spectra presented in Figure S5 indicate a marked decrease in the intensity of the excitation bands associated with the Tb^{3+} ion as the proportion of Eu^{3+} increases. This phenomenon is particularly evident for the transition from the $^7F_6 \rightarrow {}^5L_{10}$ band observed at $\lambda = 368$ nm. Such trends highlight competitive interactions between the rare earth ions and suggest a potential energy transfer mechanism [84].

The luminescence decay curves in Figure 7 indicate that the compounds exhibit phosphorescent properties, as they show lifetimes on the order of milliseconds. This is particularly evident in the monitoring of the Tb^{3+} $^5D_4 \rightarrow {}^7F_5$ transition for compounds **1**, **2**, and **5**, as well as the Eu^{3+} $^5D_0 \rightarrow {}^7F_2$ transition in compound **7**. Notably, an increase in the amount of Eu^{3+} correlates with a decrease in the Tb^{3+} lifetime, thereby confirming the occurrence of energy transfer from Tb^{3+} to Eu^{3+} [85] (Table 3).

Mono and bimetallic compounds demonstrate high quantum yields, specifically 70% for compound **1** and 68% for compound **2**, whereas the yield for compound **7** decreases to 45% (Table 3). The energy transfer efficiency from $Tb^{3+} \rightarrow Eu^{3+}$ was quantitatively analyzed utilizing Equation (1) [86]:

$$\eta_{ET} = \left[1 - \frac{\tau}{\tau_0}\right] \times 100 \quad (1)$$

where τ represents the luminescence lifetime of Tb^{3+} in the presence of Eu^{3+}, and τ_0 denotes the luminescence lifetime of Tb^{3+} in the absence of Eu^{3+}. The calculated η_{ET} values indicate a significant energy transfer efficiency of 58.8% for compound **2** and of 24.3% for compound **5**. These findings suggest that energy transfer is markedly more efficient at lower concentrations of Eu^{3+}, implying that higher concentrations may induce Eu-Eu cross-relaxation phenomena, which consequently lead to luminescence quenching. Given that the concentration of Eu^{3+} ions in compound **5** is 30%, a considerable fraction of these ions may be situated exclusively among neighboring Eu^{3+} ions.

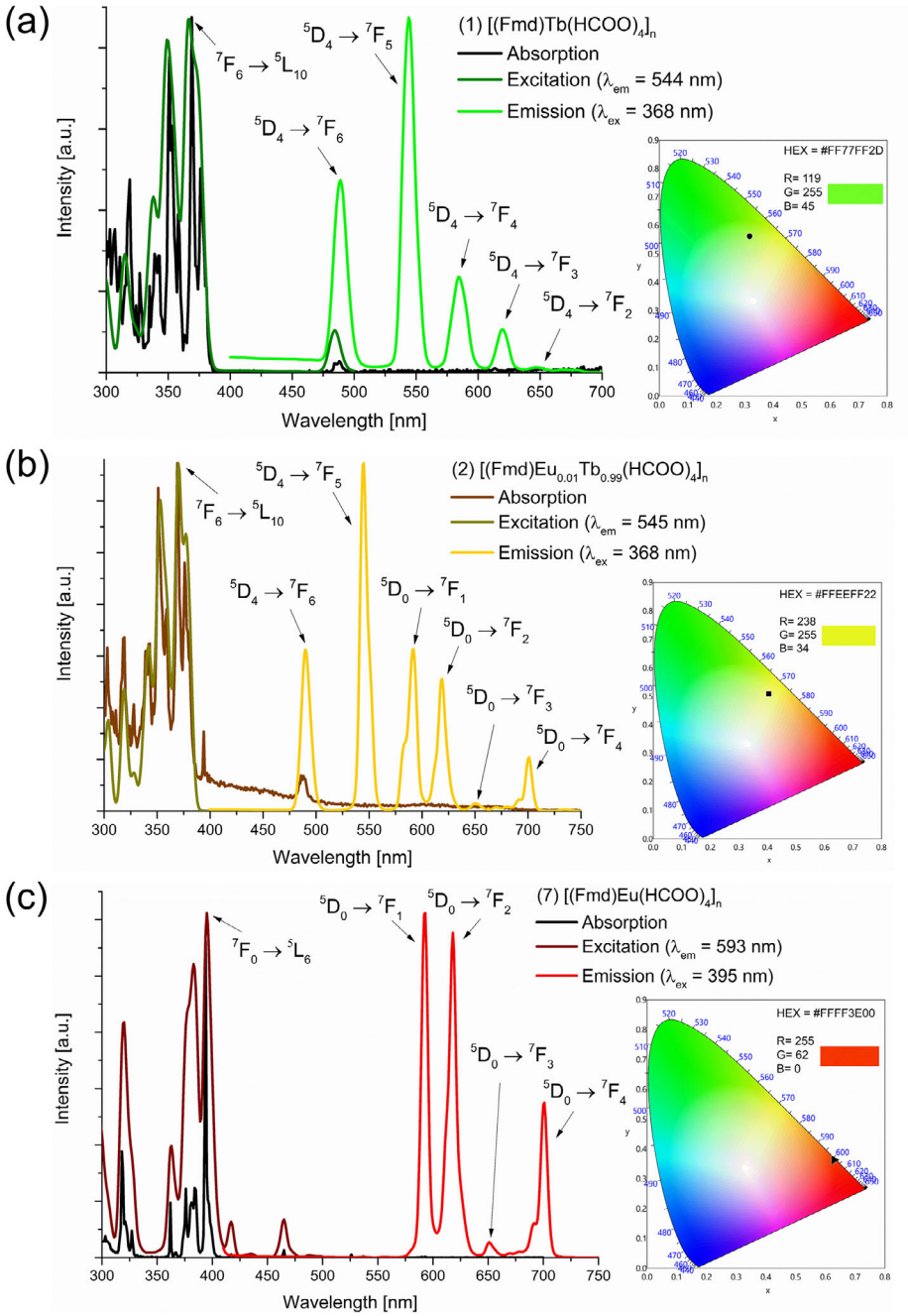

FIGURE 5 | Normalized solid state absorption, excitation, emission spectra and CIE diagrams for compounds 1 (a), 2 (b) and 7 (c).

Consequently, this spatial arrangement places them beyond the effective interaction range of Tb^{3+} energy donors. The correlation between the quantum yield and energy transfer efficiency values is consistent with the observed experimental results. The synthesis of the EuTm and TbTm bimetallic compounds was conducted in a 50:50 molar ratio. Direct excitation of the Eu^{3+} and Tb^{3+} ions at wavelengths of 392 and 367 nm, respectively, resulted in detectable emissions from both Eu^{3+} and Tb^{3+} ions; however, the emissions from Tm^{3+} did not exhibit an increase in intensity. This observation indicates that the Eu^{3+} and Tb^{3+} ions do not function as efficient antennae, as they do not facilitate energy transfer to Tm^{3+} electronic states in the visible region. Additionally, excitation at 367 nm not only effectively excites Tb^{3+} but also results in the excitation of Tm^{3+} ($^3H_6 \rightarrow {}^1D_2$). Nevertheless, the emission intensities of both Tb^{3+} and Eu^{3+} ions show a notable decrease, suggesting that the Tm^{3+} ion does not transfer energy to either Eu^{3+} or Tb^{3+}. Therefore, the decrease in emissions is mainly attributed to cross-relaxation, see Figure S6.

3.4.2 | Trimetallic Lanthanide Formate Frameworks with Eu^{3+}, $Tb^{3+}$and Tm^{3+}

Incorporating three distinct lanthanide ions, Eu^{3+}, Tb^{3+}, and Tm^{3+} within a polymeric matrix facilitates the modulation of emission colors to achieve white light. This process leverages the red emission ($^5D_0 \rightarrow {}^7F_2$) of Eu^{3+}, the green emission ($^5D_4 \rightarrow {}^7F_5$) of Tb^{3+}, and the blue emission ($^1G_4 \rightarrow {}^3H_6$) of Tm^{3+},

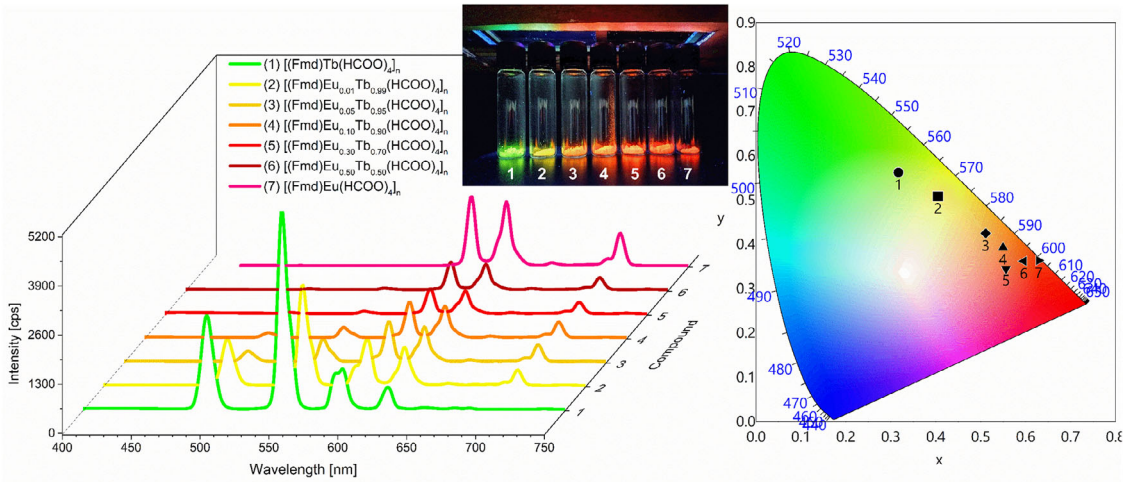

FIGURE 6 | Solid state emission spectra of the compounds $[(Fmd)Eu_xTb_{1-x}(HCOO)_4]_n$ from 1 to 7 and their location on a CIE diagram, λ_{ex} = 368 nm for 1–6, λ_{ex} = 395 nm for 7.

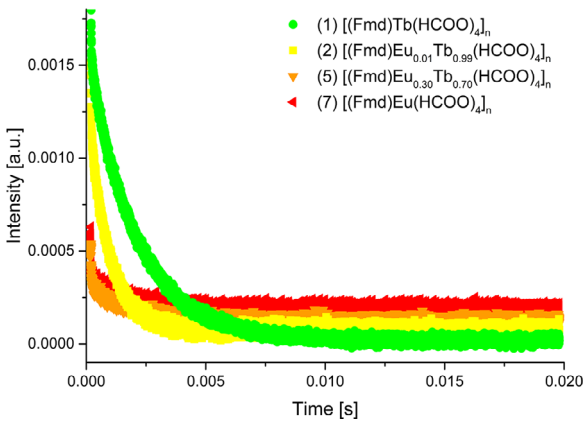

FIGURE 7 | Luminescent decay curves for compounds 1, 2, 5 and 7.

[46–54, 56, 58, 87] and the intrinsic UV-blue ligand-centered emissions of the formate ligand, associated with $n\rightarrow\pi^*$ and $\pi\rightarrow\pi^*$ transitions [88]. In ternary systems, cross-relaxation (CR) effects between lanthanide ions reduce their radiative transition rates, causing the ligand-centered emissions to become comparable in intensity to those from Eu^{3+} and Tb^{3+} [89, 90]. As shown in Figure 8a, the excitation and emission spectra of **8** and **11** confirm the origin of these ligand emissions. Upon excitation at λ = 370 nm (Figure 8b), an emission band between λ = 400 and 600 nm is observed for both, though distinct peaks from Tm^{3+} 4f–4f transitions are also present in the case of **8**. Excitation at λ = 248 nm generates the characteristic emissions of Eu^{3+} and Tb^{3+} and is attributed to a ligand-to-metal charge transfer (LMCT) band (Figure 8c,d). Similar states associated with carboxylate and acetylacetonate ligands have been described in Eu^{3+} complexes [91, 92]. Although these states may promote non-radiative deactivation processes by interfering with the singlet and triplet states involved in energy transfer, [93] in the MOFs analyzed here the formate ligands appear to provide an additional sensitization pathway, indicating that this band acts as an efficient high-energy absorption channel.

The energy transfer mechanism (ET1) is characterized by the transfer of energy from the $^5D_4$ state of Tb^{3+} to the $^5D_0$ state of Eu^{3+}, subsequently leading to the characteristic 4f–4f emissions from the Eu^{3+} ion. Additionally, a second mechanism (ET2) may be present, in which energy is transferred from the $^5L_{10}$ state of Tb^{3+} to the $^5L_6$ state of Eu^{3+}, followed by vibrational relaxation to the $^5D_0$ state. Both blue and ultraviolet emissions from Tm^{3+} are favored due to direct excitation. Consequently, the concentration of Tm^{3+} should be maintained at a lower ratio relative to the other lanthanide ions to mitigate excessive emissions from Tm^{3+}. The details of these energy transfer mechanisms are depicted in Figure 9. In the context of Tm^{3+} transitions, it is plausible that a cross-relaxation (CR) process occurs between Tm^{3+} ions and adjacent Eu^{3+} and Tb^{3+} ions. This interaction likely elucidates the relatively low intensity of the bands associated with these transitions.

Experimentally, a series of novel compounds was synthesized utilizing mixtures of the lanthanides Eu^{3+}, Tb^{3+} and Tm^{3+} in varying proportions. Emission spectra for each compound were acquired by exciting the samples at λ_{ex} = 368 nm, followed by the generation of CIE color diagrams from the corresponding emission spectra, as illustrated in Figure 10. The systematic variation of ion proportions was used to elucidate modifications in the emission bands of these lanthanides and to investigate the energy-transfer mechanisms among these ionic species. The assignment of the observed bands is detailed in Figure 10(l). The results indicated that the intensity of the emission bands is significantly influenced by the proportion of each lanthanide ion present in the compounds. Notably, Tm^{3+} and Tb^{3+} ions exhibited enhanced emission intensities. Also, these ions are being directly excited at the excitation wavelength of λ_{ex} = 368 nm, $^3H_6 \rightarrow {}^1D_2$ transition of Tm^{3+}, manifests within the ultraviolet region, specifically ranging from 345 to 375 nm excitation, contingent upon the inorganic matrix hosting the Tm^{3+} ions [94]. In examples (d) to (f), as the amount of Tb^{3+} decreases, the emissions of Eu^{3+} increase, indicating a significant energy transfer and the reduction of luminescence quenching through

TABLE 3 | Luminescent and color properties for the main compounds discussed in this work.

Compound	Quantum yield (φ, %)	Lifetime (τ, ms,)	Color (CIE 1931-X,Y)	RGB	CCT (K)	CRI
1, ●	70.0 (368 nm)	$1.36 \pm 1.68 \times 10^{-3}$ (544 nm)	(0.3170, 0.5623)	(119 255 48)	5796	24
2, ■	68.0 (368 nm)	$0.56 \pm 1.63 \times 10^{-3}$ (544 nm)	(0.4049, 0.5086)	(238 255 34)	4185	52
3, ◆	ND	ND	(0.5111, 0.4249)	(254 150 31)	2212	72
4, ▲	ND	ND	(0.5496, 0.3940)	(255 117 29)	1718	55
5, ▼	ND	$1.03 \pm 9.38 \times 10^{-3}$ (544 nm)	(0.5562, 0.3467)	(255 87 66)	1425	32
6, ◄	ND	ND	(0.5958, 0.3624)	(255 79 16)	1304	25
7, ►	45.0 (395 nm)	$0.99 \pm 9.95 \times 10^{-3}$ (614 nm)	(0.6290, 0.3637)	(255 62 0)	1168	8
9, ▮	4.0 (368 nm)	ND	(0.3198, 0.3027)	(255 218 246)	6276	91
10, +	26.0 (368 nm)	ND	(0.3389, 0.3591)	(255 243 213)	5256	83

*ND = Not determined.

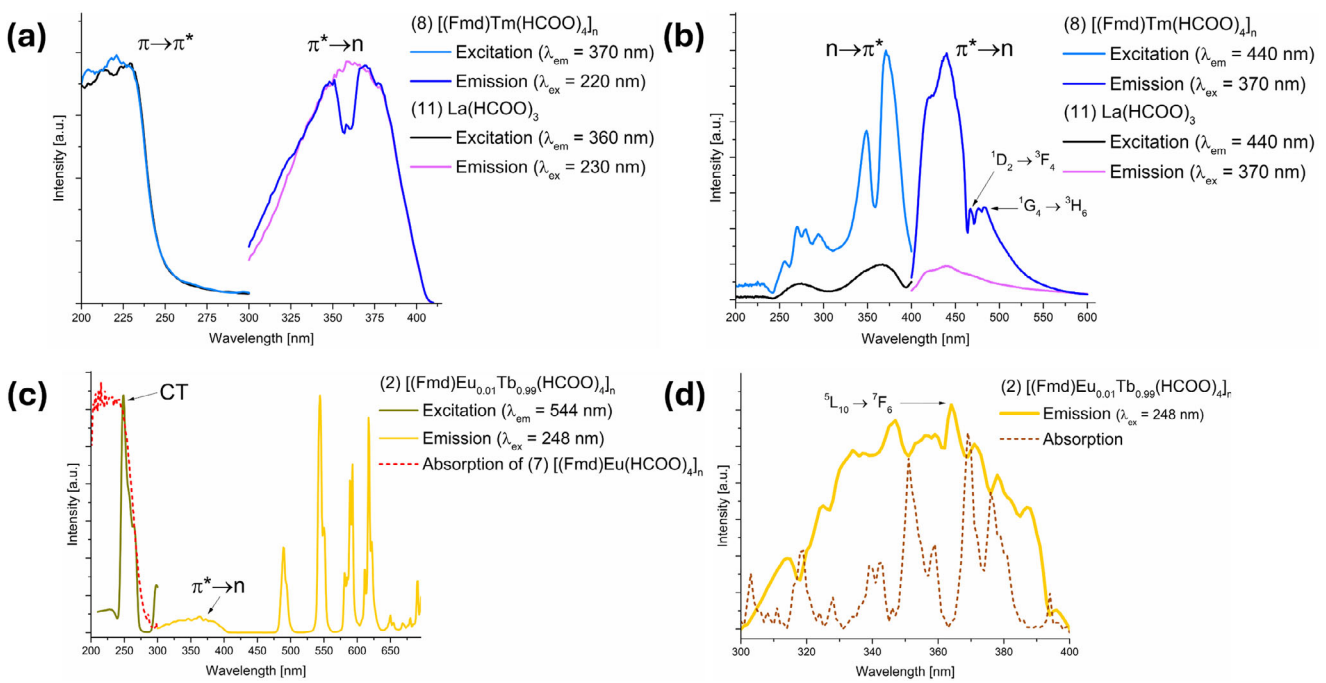

FIGURE 8 | Emission spectra. UV transitions of 8 and 11 (a), UV–vis transitions (b), Charge Transfer band $O^{2-} \rightarrow Eu^{3+}$ (c), and zoom between λ = 300 and 400 nm and its assignment to Eu^{3+} transitions (d).

the cross-relaxation mechanism. Furthermore, in section (h), where equal proportions of all three lanthanides are present, the hypersensitive band $^5D_4 \rightarrow {}^7F_5$ of Tb^{3+} and the $^1D_2 \rightarrow {}^3H_6$ band of Tm^{3+} exhibited the highest emission intensities, while $^5D_0 \rightarrow {}^7F_2$ from Eu^{3+} was significantly diminished. Additionally, it became evident that maintaining equal proportions of Tb^{3+} and Eu^{3+} while incorporating a smaller proportion of Tm^{3+} is essential for achieving white light emission, as demonstrated in sections (k) and (l). In these examples, the compound in section (l) (**9**), containing 5% Tm^{3+}, 47.5% Tb^{3+}, and 47.5% Eu^{3+}, exhibited a correlated color temperature (CCT) of 6273 K and a color rendering index (CRI) of 91. Despite the successful generation of white light with favorable CCT and CRI values, the quantum yield declined significantly compared to the mono-metallic MOFs.

3.4.3 | Effect of La^{3+} as "Diluent"

Although compound **9** displays emission characteristics that are close to the white light emission target, its intensity is

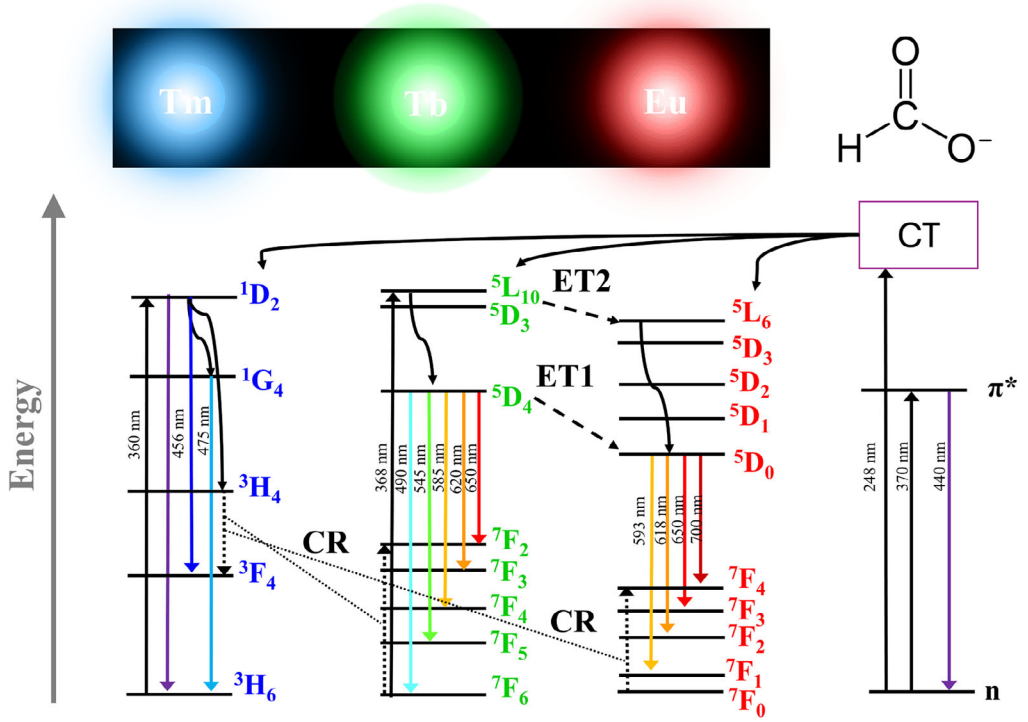

FIGURE 9 | Energy level diagrams depicting the $\lambda = 368$ nm excitation route and the routes for radiative emissions and energy transfers (dashed arrows) occurring from $Tb^{3+} \rightarrow Eu^{3+}$ (ET 1), and $Tb^{3+} \rightarrow Eu^{3+}$ (ET 2) in the trimetallic compounds.

relatively low with $\varphi = 4\%$. This may be attributed to the cross-relaxation process occurring among the three ions. Crucially, two factors are necessary in facilitating energy transfer: the interionic distance [95] and the ions' molar ratios [85]. Single-crystal x-ray diffraction studies have indicated that the minimum ion distances vary: $d_{Eu\text{-}Eu}$ = (6.714–6.832 Å) in **7**, $d_{Tb\text{-}Tb}$ = (6.694–7.000 Å) in **1**, and $d_{Tm\text{-}Tm}$ = (6.622–6.720 Å) in **8** within their respective crystals. Critical distances around 6.7 Å have been reported where lanthanide ions transfer energy efficiently in MOFs [95]. These distances appear to be optimal for preventing cross-relaxation; however, the coexistence of the three lanthanides in a single crystal facilitates quenching through this phenomenon. To solve this problem, literature evidence suggests to introduce La^{3+} ions. Non-emissive Lanthanum acts as a "diluent" for the Eu^{3+}, Tb^{3+}, and Tm^{3+} ions, thereby reducing the energy loss associated with their cross-relaxation [59, 60]. Following this idea, we prepared compound **10** with the metal proportions: 0.5% Tm^{3+}, 4.75% Tb^{3+}, 4.75% Eu^{3+} and 90% La^{3+}. However, despite the synthesis being carried out under identical conditions, we isolated a different trigonal phase (space group *R3m*) [96] $La(HCOO)_3$ doped with terbium, europium and thulium, as evidenced by the PXRD studies presented in Section 3.1 and Figure 2. Nevertheless, this different compound retained its desirable luminescent properties, resulting in a novel material exhibiting better emission intensities from Eu^{3+}, Tb^{3+} and Tm^{3+} ions with $\varphi = 26\%$. This adjustment resulted in the compound depicted in Figure 11, which shows emissions closer to warm white with increased intensity, featuring color coordinates of (0.3389, 0.3591), a CRI of 83, and a CCT of 5255 K (Table 3).

4 | Conclusion

A large family of lanthanide formate metal-organic frameworks incorporating Eu^{3+}, Tb^{3+}, and Tm^{3+} has been systematically synthesized and structurally characterized, providing a well-defined platform for investigating interionic energy transfer in rare-earth-based materials. The isostructural orthorhombic frameworks $[(Fmd)Ln(HCOO)_4]_n$ (Ln = Eu, Tb, Tm) exhibit short Ln–Ln separations (ca. 6.6–6.8 Å), which enable efficient 4f–4f energy transfer while preserving high crystallinity and thermal stability. In the bimetallic series $[(Fmd)Eu_xTb_{1\text{-}x}(HCOO)_4]_n$, a highly efficient $Tb^{3+} \rightarrow Eu^{3+}$ energy transfer process was confirmed by lifetime shortening and emission modulation, reaching a maximum transfer efficiency of 58.8% and quantum yields up to 70%. The progressive substitution of Tb^{3+} by Eu^{3+} allows continuous color tuning from green to red, demonstrating the compositional control of emission in lanthanide formate frameworks. Extension to trimetallic systems incorporating Tm^{3+} enabled RGB balance and near white emission. The composition $[(Fmd)Eu_{0.475}Tb_{0.475}Tm_{0.05}(HCOO)_4]_n$ produced chromaticity coordinates close to pure white (CIE: 0.3198, 0.3027; CRI = 91). However, the coexistence of three emissive ions promotes cross-relaxation processes that significantly reduce the quantum yield ($\varphi = 4\%$). To mitigate concentration quenching, La^{3+} was introduced as a non-emissive diluent. This modification induces a structural transformation from an orthorhombic to a new trigonal $La(HCOO)_3$ phase in which the emissive ions are statistically dispersed within a La^{3+} matrix. The increased spatial separation between active centers suppresses cross relaxation and provides

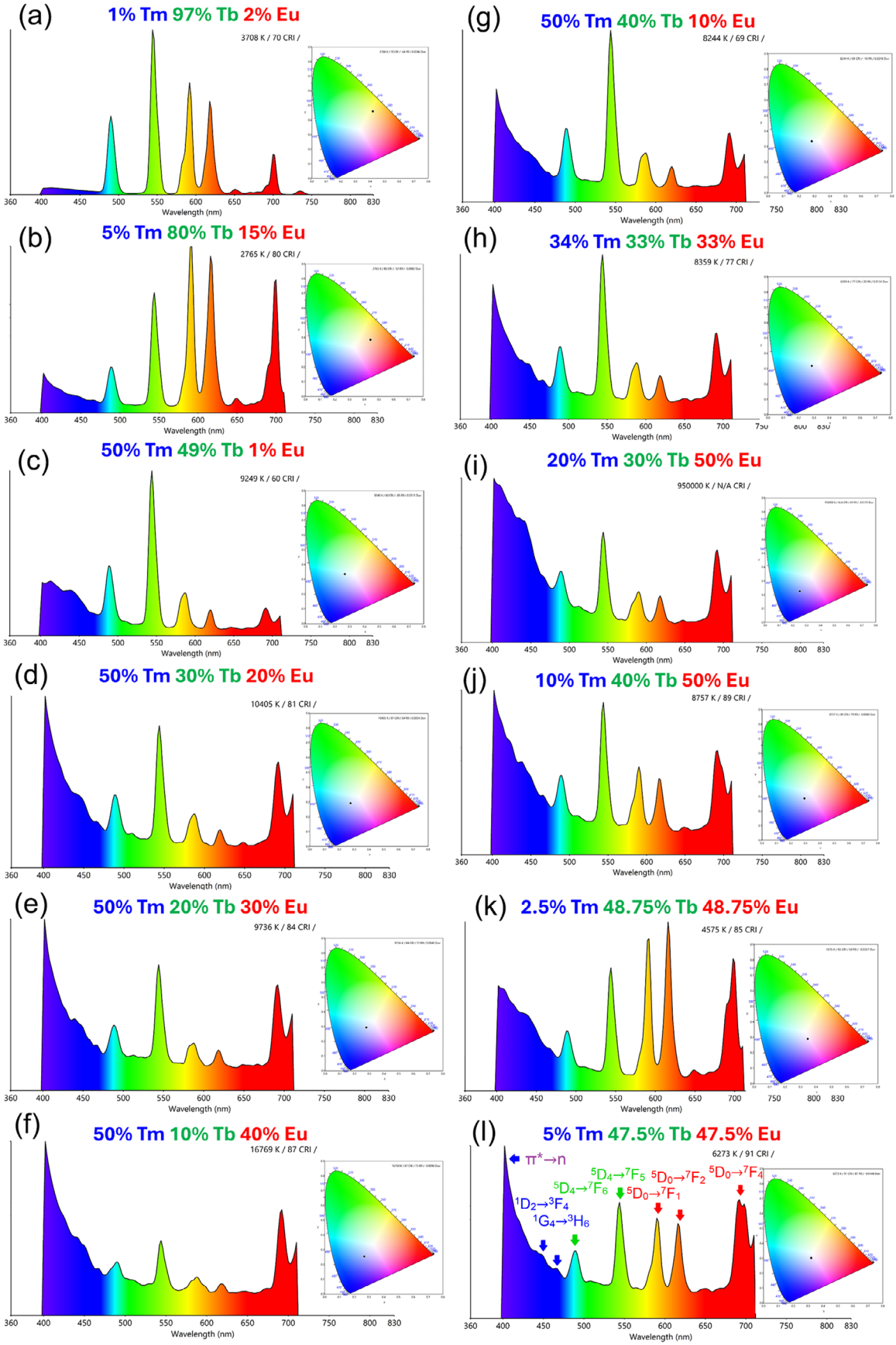

FIGURE 10 | Emission spectra of trimetallic compounds and their corresponding CIE diagrams, $\lambda_{ex} = 368$ nm.

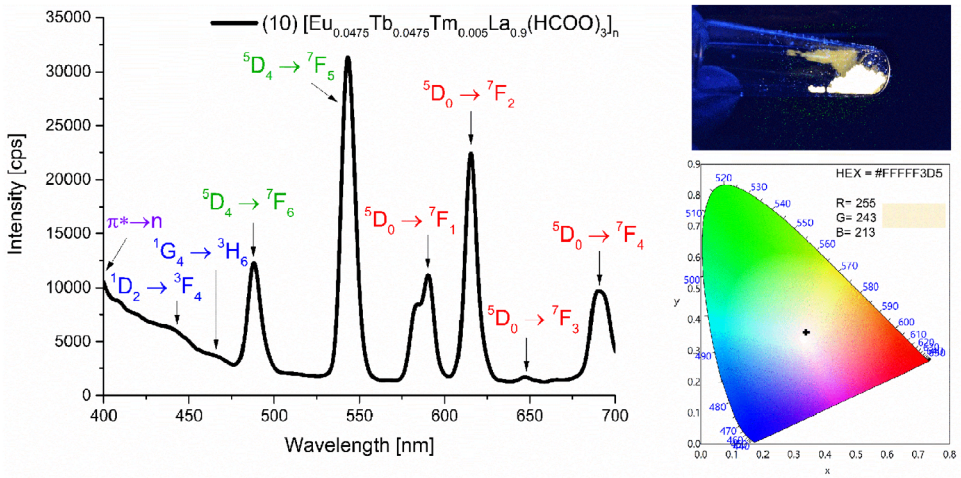

FIGURE 11 | Emission spectrum of compound 10 and its CIE diagram, $\lambda_{ex} = 368$ nm.

a compound with better quantum yield (26%), while maintaining warm white emission (CIE: 0.3389, 0.3591; CRI = 83). Overall, this work demonstrates that lanthanide formate systems provide a structurally simple yet effective model for correlating lanthanide distribution, interionic distance, and energy transfer efficiency. The results highlight the importance of both compositional tuning and structural control in the design of rare earth based white emitting materials and offer insights for future optimization of multi-lanthanide phosphors.

Author Contributions

From Contributor Role Taxonomy (CRediT) resource. L.E.C.E. Synthesis of the compounds, investigation, conceptualization, data analysis, writing and editing. I.D.V.G. Investigation, data analysis, writing. G.G. validation; C.F. Investigation, data analysis. S.E.C.B. Project administration, supervision, review and editing. A.R. Design of the molecules, project administration, supervision, writing, review and editing.

Acknowledgements

S.E.C.B. acknowledges financial support from DGAPA-PAPIIT IN227523 and PAIP 50009036 projects. We also thank the USAII UNAM technicians for support in the data collection: N. López-Balbiaux, V. H. Lemus-Neri, M. Gutiérrez-Franco, R. I. Puente-Lee. We also thank M. Romero-Ávila, H. Desirena-Enrriquez, A. Tejeda-Cruz and E. Reyes-Morales for the loan of the fluorometer, the determination of luminescent decay curves, XRD diffraction experiments, and TGA analysis, respectively. We acknowledge Dr. K.P. Salas-Martin for the technical support. We thank M.A. Armienta-Hernández, M de J. González-Guadarrama and O. Neri-Hernández for the studies carried out in ICP-OES. The authors thank M. Guerrero-Cruz for the powder diffraction pattern measurements. L.E.C.E. thanks CONAHCyT for the studentship with CVU 734200 and the Postgraduate UNAM Program for the scholarship received for the research stay at ICCOM-CNR (Florence). Dr. Giulio Bicchierai, Dr. Zeinab Saki and Dr. Giacomo Provinciali (CNR-ICCOM) are gratefully acknowledged for help in the laboratory activities during L.E.C.E. stay in Florence.

Open access publishing facilitated by Consiglio Nazionale delle Ricerche, as part of the Wiley - CRUI-CARE agreement.

Conflicts of Interest

The authors declare no conflicts of interest.

Data Availability Statement

The data that supports the findings of this study are available in the supplementary material of this article.

References

1. M. Farooq, H. Rafiq, A. I. Shah, and M. H. Rasool, "On the Development Of Phosphors For Luminescent Materials: Synthesis, Characterization, Applications And Evolution Of Phosphors As White-Light-Emitting Diodes," *ECS Journal of Solid State Science Technology* 12 (2023): 126002.

2. L. Chen, C. C. Lin, C. W. Yeh, and R. S. Liu, "Light Converting Inorganic Phosphors For White Light-Emitting Diodes," *Materials* 3 (2010): 2172–2195.

3. N. C. Chiu, K. T. Smith, and K. C. Stylianou, "Metal-Organic Frameworks For White Light Emission: From Synthesis To Device Fabrication," *Coordination Chemistry Reviews* 459 (2022): 214441.

4. A. Karmakar and J. Li, "Luminescent MOFs (LMOFs): Recent advancement towards a greener WLED Technology," *ChemComm* 58 (2022): 10768.

5. H. Wu, H. Li, L. Jiang, et al., "Design of White-Emitting Optical Temperature Sensor Based On Energy Transfer in a Bi^{3+}, Eu^{3+} and Tb^{3+} doped YBO_3 Crystal," *Journal of Materials Chemical C Materials* 9 (2021): 7264–7273.

6. H. Li, J. Zheng, Y. Dai, et al., "Low-Cost Dual-Emissive Phosphors With UV-to-visible Persistent Luminescence For Information Encryption And Advanced Anti-Counterfeiting," *Ceramics International* 51 (2025): 49701–49712.

7. S. Ashwini, S. C. Prashantha, R. Naik, H. Nagabhushana, D. M. Jnaneshwara, and K. N. Narasimhamurthy, "Bi_2O_3:Dy_{3+} Nanophosphors: Its White Light Emission And Photocatalytic Activity," *SN Applied Science* 1 (2019): 1028.

8. K. Panigrahi and A. Nag, "Challenges and Strategies To Design Phosphors For Future White Light Emitting Diodes," *Journal of Physical Chemistry C* 126 (2022): 8553–8564.

9. M. Sato, S. W. Kim, Y. Shimomura, T. Hasegawa, K. Toda, and G. Adachi, *Handbook on the Physics and Chemistry of Rare Earths* (Elsevier, 2016).

10. S. N. Zhao, G. Wang, D. Poelman, and P. Van Der Voort, "Luminescent lanthanide MOFs: A Unique Platform For Chemical Sensing," *Materials* 11 (2018): 572.

11. R. Li, L. Li, W. Zi, et al., "Morphology control and multicolor-tunable luminescence of YOF: Ln^{3+} (Ln= Eu, Tb, Dy, Tm) nano-/microcrystals," *New Journal of Chemistry* 39 (2015): 115–121.

12. D. Parker, E. A. Suturina, I. Kuprov, and N. F. Chilton, "How the Ligand Field In Lanthanide Coordination Complexes Determines Magnetic Susceptibility Anisotropy, Paramagnetic NMR Shift, And Relaxation Behavior," *Accounts of Chemical Research* 53 (2020): 1520–1534.

13. S. V. Eliseeva and J. C. G. Bünzli, "Lanthanide Luminescence For Functional Materials And Bio-Sciences," *Chemical Society Reviews* 39 (2010): 189–227.

14. Y. Zhang, S. Yuan, G. Day, X. Wang, X. Yang, and H. C. Zhou, "Luminescent Sensors Based On Metal-Organic Frameworks," *Coordination Chemistry Reviews* 354 (2018): 28–45.

15. M. Runowski, N. Stopikowska, and S. Lis, "UV–vis–NIR Absorption Spectra Of Lanthanide Oxides And Fluorides," *Dalton Transactions* 49 (2020): 2129–2137.

16. L. Armelao, S. Quici, F. Barigelletti, et al., "Design of Luminescent Lanthanide Complexes: From Molecules To Highly Efficient Photo-Emitting Materials," *Coordination Chemistry Reviews* 254 (2010): 487–505.

17. R. Zhang, L. Zhu, and B. Yue, "Luminescent Properties And Recent Progress In Applications Of Lanthanide Metal-Organic Frameworks," *Chinese Chemical Letters* 34 (2023): 108009.

18. C. Wegeberg and O. S. Wenger, "Luminescent First-Row Transition Metal Complexes," *JACS Au* 1 (2021): 1860–1876.

19. J. Heine and K. Müller-Buschbaum, "Engineering Metal-Based Luminescence In Coordination Polymers And Metal–Organic Frameworks," *Chemical Society Reviews* 42 (2013): 9232.

20. Y. Cui, Y. Yue, G. Qian, and B. Chen, "Luminescent Functional Metal–Organic Frameworks," *Chemical Reviews* 112 (2012): 1126–1162.

21. J. Dong, D. Zhao, Y. Lu, and W. Y. Sun, "Photoluminescent Metal–Organic Frameworks And Their Application For Sensing Biomolecules," *Journal of Materials Chemistry A* 7 (2019): 22744–22767.

22. M. D. Allendorf, C. A. Bauer, R. K. Bhakta, and R. J. T. Houk, "Luminescent Metal–Organic Frameworks," *Chemical Society Reviews* 38 (2009): 1330.

23. M. Pamei and A. Puzari, "Luminescent Transition Metal–Organic Frameworks: An Emerging Sensor For Detecting Biologically Essential Metal Ions," *Nano-Structure and Nano-Objects* 19 (2019): 100364.

24. L. Chen, D. Liu, J. Peng, Q. Du, and H. He, "Ratiometric Fluorescence Sensing Of Metal-Organic Frameworks: Tactics and Perspectives," *Coordination Chemistry Reviews* 404 (2020): 213113.

25. Y. Cui, J. Zhang, B. Chen, and G. Qian, *Handbook on the Physics and Chemistry of Rare Earths* (Elsevier, 2016).

26. K. Patra and H. Pal, "Lanthanide-Based Metal–Organic Frameworks (Ln-MOFs): Synthesis, Properties And Applications," *RSC Sustainability* 3 (2025): 629–660.

27. W. P. Lustig and J. Li, "Luminescent Metal–Organic Frameworks And Coordination Polymers As Alternative Phosphors For Energy Efficient Lighting Devices," *Coordination Chemistry Reviews* 373 (2018): 116–147.

28. G. Lorusso, J. W. Sharples, E. Palacios, et al., "A Dense Metal–Organic Framework For Enhanced Magnetic Refrigeration," *Advanced Materials* 25 (2013): 4653–4656.

29. Z. Han, Y. Yang, J. Rushlow, et al., "Development of the Design And Synthesis Of Metal–Organic Frameworks (MOFs)–from Large Scale Attempts, Functional Oriented Modifications, To Artificial Intelligence (AI) Predictions," *Chemical Society Reviews* 54 (2024): 367–395.

30. X. Ma, X. Xu, F. Duan, W. Huang, Q. Chen, and D. Wu, "High-Efficiency Wideband Excitable Mechanoluminescence from a Yellow MOF Phosphor as White LED and Multicolor Thin Films," *Advanced Optical Materials* 10 (2022): 2101461.

31. L. Xu, Y. Xu, X. Li, Z. Wang, T. Sun, and X. Zhang, "Eu^{3+}/Tb^{3+} Functionalized Bi-Based Metal–Organic Frameworks Toward Tunable White-Light Emission And Fluorescence Sensing Applications," *Dalton Transactions* 47 (2018): 16696–16703.

32. M. Gutiérrez, Y. Zhang, and J. C. Tan, "Confinement of Luminescent Guests In Metal–Organic Frameworks: Understanding Pathways From Synthesis And Multimodal Characterization To Potential Applications of LG@ MOF Systems," *Chemical Reviews* 122 (2022): 10438.

33. D. Li, A. Yadav, H. Zhou, K. Roy, P. Thanasekaran, and C. Lee, "Advances and Applications Of Metal-Organic Frameworks (MOFs) in Emerging Technologies: A Comprehensive Review," *Global Challenges* 8 (2024): 2300244.

34. J. E. Ellis, S. E. Crawford, and K. J. Kim, "Metal–Organic Framework Thin Films As Versatile Chemical Sensing Materials," *Materials Advances* 2 (2021): 6169–6196.

35. V. Haquin, M. Etienne, C. Daiguebonne, et al., "Color and Brightness Tuning In Heteronuclear Lanthanide Terephthalate Coordination Polymers," *European Journal of Inorganic Chemistry* (2013): 3464–3476.

36. A. E. Psalti, D. Andriotou, S. A. Diamantis, et al., "Mixed-metal and mixed-ligand Lanthanide Metal–Organic frameworks based on 2, 6-Naphthalenedicarboxylate: Thermally activated sensitization and White-Light Emission," *Inorganic Chemistry* 61 (2022): 11959–11972.

37. Y. Tang, H. Wu, W. Cao, Y. Cui, and G. Qian, "Luminescent Metal–Organic Frameworks For White LEDs," *Advanced Optical Materials* 9 (2021): 2001817.

38. S. Zou, Q. Li, and S. Du, "Efficient and Tunable Multi-Color and White Light Ln-MOFs with High Luminescence Quantum Yields," *RSC Advances* 5 (2015): 34936–34941.

39. S. Xing and C. Janiak, "Design and Properties Of Multiple-Emitter Luminescent Metal–Organic Frameworks," *ChemComm* 56 (2020): 12290.

40. J. J. Perry IV, C. A. Bauer, and M. D. Allendorf, "Luminescent Metal-Organic Frameworks,", in *Metal-Organic Frameworks: Applications from Catalysis to Gas Storage*, ed: D. Farrusseng, Wiley VCH (2011): 267–308.

41. G. Mercuri, G. Giambastiani, and A. Rossin, "Thiazole-and Thiadiazole-Based Metal–Organic Frameworks and Coordination Polymers for Luminescent Applications," *Inorganics* 7 (2019): 144.

42. H. A. Bicalho, L. A. Trifoi, V. Quezada-Novoa, and A. J. Howarth, "Tuning the Photophysical and Photochemical Properties of Rare-Earth Cluster-Based Metal–Organic Frameworks," *ACS Applied Electronic Materials* 6 (2024): 7055–7064.

43. J. Xue, Y. Wang, G. Yang, and Y. Wang, "Energy Transfer, Anticounterfeiting, White Light Emission And Sensing In Fine-Regulating Series Of Lanthanide Metal-Organic Frameworks," *Journal of Rare Earths* 42 (2024): 446–454.

44. L. L. Ma, G. P. Yang, G. P. Li, et al., "Luminescence Modulation, Near White Light Emission, Selective Luminescence Sensing, And Anticounterfeiting Via A Series of Ln-MOFs with a π-Conjugated And Uncoordinated Lewis Basic Triazolyl ligand," *Inorganic Chemistry Frontier* 8 (2021): 329–338.

45. Z. Ajoyan, H. A. Bicalho, P. R. Donnarumma, A. Antanovich, and A. J. Howarth, "Tuning the Rare-Earth UiO-66 Metal–Organic Framework Platform For White Light Emission," *Journal of Materials Chemistry C* 11 (2023): 8929–8934.

46. I. Kashif and A. Ratep, "Various Color Light Emission from Single, Double, and Triple $Eu^{3+}/Tb^{3+}/Tm^{3+}$ Doped Borate Glass Excited by UV Light," *Journal of Fluorescence* 35 (2025): 343–355.

47. V. Naresh, K. Gupta, C. P. Reddy, and B. S. Ham, "Energy Transfer And Colour Tunability in UV Light Induced $Tm^{3+}/Tb^{3+}/Eu^{3+}$: ZnB Glasses Generating White Light Emission," *Spectrochimica Acta Part A, Molecular and Biomolecular Spectroscopy* 175 (2017): 43–50.

48. C. J. Zhao, J. L. Cai, R. Y. Li, S. L. Tie, X. Wan, and J. Y. Shen, "White Light Emission from $Eu^{3+}/Tb^{3+}/Tm^{3+}$ Triply-Doped Aluminoborate Glass Excited by UV light," *Journal of Non-Crystalline Solids* 358 (2012): 604–608.

49. X. Huo, Z. Wang, C. Tao, et al., "Single-Component White Emitting Phosphor $Mg_2Y_2Al_2Si_2O_{12}$: Tb^{3+}, Eu^{3+}, Tm^{3+} for white LEDs," *Journal of Alloys and Compounds* 902 (2022): 163823.

50. X. Liu, W. Hou, X. Yang, and J. Liang, "Morphology Controllable Synthesis of NaLa $(WO_4)_2$: The Morphology Dependent Photoluminescent Properties And Single-Phased White Light Emission of NaLa $(WO_4)_2$: $Eu^{3+}/Tb^{3+}/Tm^{3+}$," *CrystEngComm* 16 (2014): 1268.

51. Q. Ren, Y. Zhao, X. Wu, and O. Hai, "$Tb^{3+}/Eu^{3+}/Tm^{3+}$ co-Doped Single-Phase Phosphors Emitting Close To Standard White Light," *Optics & Laser Technology* 136 (2021): 106774.

52. Z. Yahiaoui, M. A. Hassairi, M. Dammak, and E. Cavalli, "Tunable Luminescence And Near White-Light Emission of YPO_4: Eu^{3+}, Tb^{3+}, Tm^{3+} Phosphors," *Journal of Alloys and Compounds* 763 (2018): 56–61.

53. A. S. Kuznetsov, A. Nikitin, V. K. Tikhomirov, M. V. Shestakov, and V. V. Moshchalkov, "Ultraviolet-Driven White Light Generation From Oxyfluoride Glass Co-Doped with Tm^{3+}-Tb^{3+}-Eu^{3+}," *Applied Physics Letters* 102 (2013): 161916.

54. L. X. Lovisa, V. D. Araújo, R. L. Tranquilin, et al., "White Photoluminescence Emission from ZrO_2 co-Doped with Eu^{3+}, Tb^{3+} and Tm^{3+}," *Journal of Alloys and Compounds* 674 (2016): 245–251.

55. W. Ma, Z. Shi, and R. Wang, "Luminescence Properties Of Full-Color Single-Phased Phosphors For White LEDs," *Journal of Alloys and Compounds* 503 (2010): 118–121.

56. Y. Li, Y. Cai, C. Ming, et al., "Simple Synthesis, Adjusting Luminescence Colour And White Light Emission of Ln^{3+}:CeF_3 (Ln = Tm, Tb, Eu) Phosphors," *Bulletin of Materials Science* 46 (2023): 113.

57. M. Mungra, F. Steudel, B. Ahrens, and S. Schweizer, "Tm/Tb/Eu Triple-Doped Lithium Aluminoborate Glass For White Light Generation," *Journal of Luminescence* 192 (2017): 71–76.

58. N. Ravina, K. Poria, M. K. Sahu, et al., "Energy Transfer Mechanisms And Color-Tunable Luminescence of $Tm^{3+}/Tb^{3+}/Eu^{3+}$ co-Doped $Sr_4Nb_2O_9$ Phosphors For High-Quality White Light-Emitting Diodes," *RSC Advances* 13 (2023): 33675–33687.

59. Z. Si, L. Wang, J. Hu, and W. Jiang, "Enhanced Luminescence of terbium-1-cyclopropyl-6-fluoro-1, 4-dihydro-4-oxo-7-(1-piperazinyl)-3-Quinolinecarboxylic Acid With Lanthanum and its Application," *Microchemical Journal* 70 (2001): 19–24.

60. L. Zhai, W. W. Zhang, X. M. Ren, and J. L. Zuo, "Observation of divergent La^{3+} Ion Dilute Effect In Two Series of 3-D Fluorescent Lanthanide-MOFs-Based Molecular Alloys RExLa1− x–EBTC (RE3+= Eu^{3+} or Tb^{3+}; EBTC4−= 1, 1′-ethynebenzene-3, 3′, 5, 5′-etracarboxylate)," *Journal of Solid State Chemistry* 230 (2015): 14–18.

61. J. Cepeda, S. Pérez-Yáñez, G. Beobide, et al., "Exploiting Synthetic Conditions To Promote Structural Diversity within the Scandium (III)/Pyrimidine-4, 6-Dicarboxylate System," *Crystal Growth & Design* 15 (2015): 2352–2363.

62. R. S. Crees, M. L. Cole, L. R. Hanton, and C. J. Sumby, "Synthesis of a Zinc (II) Imidazolium Dicarboxylate Ligand Metal− Organic Framework (MOF): A Potential Precursor to MOF-Tethered N-Heterocyclic Carbene Compounds," *Inorganic Chemistry* 49 (2010): 1712–1719.

63. X. Ma, J. Tian, H. Y. Yang, K. Zhao, and X. Li, "3D Rare Earth Porous Coordination Frameworks With Formamide Generated In Situ Syntheses: Crystal Structure And Down-And Up-Conversion Luminescence," *Journal of Solid State Chemistry* 201 (2013): 172–177.

64. P. Samarasekere, X. Wang, W. Kaveevivitchai, and A. J. Jacobson, "Reactions of Rare Earth Hydrated Nitrates And Oxides With Formamide: Relevant To Recycling Rare Earth Metals," *Crystal Growth & Design* 15 (2015): 1119–1128.

65. A. Rossin, G. Giambastiani, M. Peruzzini, and R. Sessoli, "Amine-Templated Polymeric Lanthanide Formates: Synthesis, Characterization, And Applications In Luminescence And Magnetism," *Inorganic Chemistry* 51 (2012): 6962–6968.

66. M. C. Burla, R. Caliandro, B. Carrozzini, et al., "Crystal Structure Determination And Refinement via SIR2014," *Journal of Applied Crystallography* 48 (2015): 306–309.

67. G. M. Sheldrick, "Crystal structure refinement with SHELXL," *Acta Crystallographica Section C Structural Chemistry* 71 (2015): 3–8.

68. M. Nardelli, "PARST95–an update to PARST: A system of Fortran Routines For Calculating Molecular Structure Parameters From The Results Of Crystal Structure Analyses," *Computers & Chemistry* 7 (1983): 95–98.

69. G. L. Zhuang, X. J. Kong, L. S. Long, R. Bin Huang, and L. S. Zheng, "Effect of Lanthanide Contraction On Crystal Structures Of Lanthanide Coordination Polymers with 2, 5-Piperazinedione-1, 4-Diacetic Acid," *CrystEngComm* 12 (2010): 2691.

70. A. Atanasova, T. Hristova-Vasileva, and R. Todorov, "Influence of the Molecular Weight And Concentration of PVP on the Polyol Synthesized Silver Nanoparticles," *Journal of Physics: Conference Series* 1762 (2021): 012032.

71. K. Patel, V. Blair, J. Douglas, et al., "Structural Effects Of Lanthanide Dopants On Alumina," *Scientific Reports* 7 (2017): 39946.

72. P. Kistaiah, K. Sathyanarayana Murthy, L. Iyengar, and K. V. Krishna Rao, "X-ray Studies On The High Pressure Behaviour Of Some Rare-Earth Formates," *Journal of Materials Science* 16 (1981): 2321–2323.

73. F. M. Amombo Noa, E. S. Grape, M. Åhlén, et al., "Chiral Lanthanum Metal–Organic Framework with Gated CO_2 Sorption and Concerted Framework Flexibility," *Journal of the American Chemical Society* 144 (2022): 8725–8733.

74. A. Gómez-Avilés, J. Bedia, and C. Belver, "Hybrid Zirconium-Lanthanum Metal-Organic Frameworks For Solar-Driven Sulfamethoxazole Degradation," *Applied Catalysis B* 378 (2025): 125566.

75. A. Rossin, M. R. Chierotti, G. Giambastiani, R. Gobetto, and M. Peruzzini, "Amine-Templated Polymeric Mg Formates: Crystalline Scaffolds Exhibiting Extensive Hydrogen Bonding," *CrystEngComm* 14 (2012): 4454.

76. S. Wang, J. Xu, Y. Fan, et al., "3D Lanthanide Metal–Organic Frameworks Constructed From Lanthanide Formate Skeletons and 3, 5-bis (4′-carboxy-phenyl)-1, 2, 4-Triazole Connectors: Synthesis, Structure And Luminescence," *RSC Advances* 5 (2015): 106107–106112.

77. C. Petersen, J. Thøgersen, S. K. Jensen, and S. R. Keiding, "Investigation of the Primary Photodynamics Of The Aqueous Formate Anion," *Journal of Physical Chemistry A* 110 (2006): 3383–3387.

78. D. Y. Medina-Velazquez, U. Caldiño, A. Morales-Ramirez, et al., "Synthesis of Luminescent Terbium-Thenoyltriflouroacetone MOF Nanorods For Green Laser Application," *Opticals Materials* 87 (2019): 3–10.

79. L. Bertry, O. Durupthy, P. Aschehoug, B. Viana, and C. Chanéac, "Experimental Evidence Of Luminescence Quenching At Long Coupling Distances In Europium (III) Doped Core-Shell Gold Silica Nanoparticles," *Gold Bulletin* 46 (2013): 349–355.

80. K. Binnemans, "Interpretation of Europium (III) Spectra," *Coordination Chemistry Reviews* 295 (2015): 1–45.

81. P. A. Tanner, "Some Misconceptions Concerning The Electronic Spectra Of Tri-Positive Europium And Cerium," *Chemical Society Reviews* 42 (2013): 5090.

82. R. Peña-Rodríguez, J. A. Molina-González, H. Desirena-Enrriquez, J. M. Rivera-Villanueva, and S. E. Castillo-Blum, "Tunable Luminescence Modulation And Warm Light Emission of Zn-MOF (4, 4′-bipyridyl and zinc acetate) doped with Eu^{3+} and Tb^{3+}," *Materials Chemistry and Physics* 223 (2019): 494.

83. R. Peña-Rodríguez, J. A. Molina-González, H. Desirena-Enrriquez, E. Armenta-Jaime, J. M. Rivera, and S. E. Castillo-Blum, "Doping of a Zn-MOF with Eu^{3+} and Tb^{3+} for application in the manufacture of a WLED," *Journal of Materials Chemistry C* 9 (2021): 15891.

84. A. N. Carneiro Neto, R. T. Moura, A. Shyichuk, et al., "Theoretical and Experimental Investigation of the Tb^{3+}-> Eu^{3+} Energy Transfer Mechanisms in Cubic A (3) Tb (0.90) Eu (0.10)(PO_4)(3)(A= Sr, Ba) Materials," *Journal of Physical Chemistry C* 124 (2020): 10105–10116.

85. Z. Li, R. Nuñez, M. E. Light, et al., "Water-Stable Carborane-Based Eu^{3+}/Tb^{3+} Metal–Organic Frameworks For Tunable Time-Dependent Emission Color And Their Application In Anticounterfeiting Bar-Coding," *Chemistry of Materials* 34 (2022): 4795–4808.

86. T. Li, J. Liu, F. Jiang, et al., "Doping Gd 16 Nanoclusters For Expanded Optical Properties And Thermometry Applications," *Nanoscale* 17 (2025): 5074–5080.

87. M. Mungra, F. Steudel, B. Ahrens, and S. Schweizer, "Tm/Tb/Eu Triple-Doped Lithium Aluminoborate Glass For White Light Generation," *Journal of Luminescence* 192 (2017): 71–76.

88. M. Szyper and P. Zuman, "Electronic Absorption Of Carboxylic Acids And Their Anions," *Analytica Chimica Acta* 85 (1976): 357–373.

89. R. Lisiecki, W. Ryba-Romanowski, and T. Łukasiewicz, "Relaxation of excited states of Tm^{3+} and Tm^{3+}-Eu^{3+} Energy Transfer in YVO_4 Crystal," *Applied Physics B* 83 (2006): 255–259.

90. A. F. H. Librantz, L. Gomes, G. Pairier, S. J. L. Ribeiro, and Y. Messaddeq, "Effects in the Population Inversion of $3H_4$ level in Tm, Tm-Tb, and Tm-Eu Doped Germanate Glasses For Amplifiers Applications," *Solid State Lasers and Amplifiers II* 6190 (2006): 61901G.

91. K. P. Zhuravlev, V. I. Tsaryuk, and V. A. Kudryashova, "Photoluminescence of Europium And Terbium Trifluoroacetylacetonates. Participation of LMCT State In Processes Of The Energy Transfer to Eu^{3+} ion," *Journal of Fluorine Chemistry* 212 (2018): 137–143.

92. I. P. Assunção, A. N. Carneiro Neto, R. T. Moura, et al., "Odd-Even Effect On Luminescence Properties Of Europium Aliphatic Dicarboxylate Complexes," *ChemPhysChem* 20 (2019): 1931.

93. E. Kasprzycka, A. N. Carneiro Neto, V. A. Trush, et al., "How Minor Structural Changes Generate Major Consequences In Photophysical Properties Of Re Coordination Compounds; Resonance Effect, LMCT state," *Journal of Rare Earths* 38 (2020): 552–563.

94. N. O. Etafo, "Interpretation and Applications of Tm^{3+} Spectra: From Energy Levels To Photonic Devices," *Coordination Chemistry Reviews* 557 (2026): 217717.

95. L. L. Da Luz, B. F. Lucena Viana, G. C. O. Da Silva, et al., "Controlling the Energy Transfer In Lanthanide–Organic Frameworks For The Production Of White-Light Emitting Materials," *CrystEngComm* 16 (2014): 6914.

96. J. M. Lin, Y. F. Guan, D. Y. Wang, W. Dong, X. T. Wang, and S. Gao, "Syntheses, Structures And Properties Of Seven Isomorphous 1D Ln^{3+} complexes Ln (BTA)$(HCOO)(H_2O)_3$ (H_2 BTA= bis (tetrazoly) amine, Ln= Pr, Gd, Eu, Tb, Dy, Er, Yb) and two 3D Ln^{3+} complexes Ln $(HCOO)_3$ (Ln= Pr, Nd)," *Dalton Transactions* 37 (2008): 6165–6169.

Supporting Information

Additional supporting information can be found online in the Supporting Information section.

Supporting File: adom71447-sup-0001-SuppMat.pdf.